

Article

Characterizing the Dissolution Rate of CO₂-Brine in Porous Media under Gaseous and Supercritical Conditions

Bohao Wu ¹ , Xingbo Li ¹, Ying Teng ¹, Pengfei Lv ¹, Yu Liu ¹, Tingting Luo ¹, Jianan Zheng ¹, Dayong Wang ¹ and Lanlan Jiang ^{1,2,*}

¹ Key Laboratory of Ocean Energy Utilization and Energy Conservation of Ministry of Education, Dalian University of Technology, Dalian 116024, China; 603336164@mail.dlut.edu.cn (B.W.); lixb1988@mail.dlut.edu.cn (X.L.); tywzb@mail.dlut.edu.cn (Y.T.); lvpf910@mail.dlut.edu.cn (P.L.); liuyu@dlut.edu.cn (Y.L.); ligonglitt@mail.dlut.edu.cn (T.L.); zhengjn@mail.dlut.edu.cn (J.Z.); wangdy@dlut.edu.cn (D.W.)

² Research Institute of Innovative Technology for the Earth, Kizugawa City, Kyoto 619-0292, Japan

* Correspondence: lanlan@dlut.edu.cn; Tel.: +86-0411-8470-8015

Received: 28 November 2017; Accepted: 18 December 2017; Published: 21 December 2017

Abstract: The CO₂-brine dissolution homogenizes the distribution of residual CO₂ and reduces the leakage risk in the saline aquifer. As a key parameter to immobilize the free CO₂, the dissolution rate of CO₂-brine could be accelerated through mechanisms like diffusion and dispersion, which are affected by the subsurface condition, pore structure, and background hydrological flow. This study contributed the calculated dissolution rates of both gaseous and supercritical CO₂ during brine imbibition at a pore-scale. The flow development and distribution in porous media during dynamic dissolution were imaged in two-dimensional visualization using X-ray microtomography. The fingerings branching and expansion resulted in greater dissolution rates of supercritical CO₂ with high contact between phases, while the brine bypassed the clusters of gaseous CO₂ with a slower dissolution and longer duration due to the isolated bubbles. The dissolution rate of supercritical CO₂ was about two or three orders of magnitude greater than that of gaseous CO₂, while the value distributions both spanned about four orders of magnitude. The dissolution rates of gaseous CO₂ increased with porosity, but the relationship was the opposite for supercritical CO₂. CO₂ saturation and the Reynolds number were analyzed to characterize the different impacts on gaseous and supercritical CO₂ at different dissolution periods.

Keywords: porous media; CO₂ storage; dissolution rate; heterogeneity; micro-computed tomography

1. Introduction

The residual and solubility trapping of CO₂ in the saline aquifer maximize the storage capacity and ensure the reservoir integrity of CO₂ sequestration [1]. After CO₂ is injected into target reservoirs, it migrates in permeable rock under a supercritical state and dissolves into brine to form carbonic acid [2]. The dissolution process reduces the risk of CO₂ leakage through the caprock of the reservoir due to the upward movement of the CO₂ plume under the buoyancy effect [3]. The dissolution rate of CO₂-brine, which represents the mass transfer process, serves as an important parameter to immobilize the free-phase CO₂.

The major driving force of the dissolution rate is the partitioning non-equilibrium concentration and is controlled by the interfacial and environmental conditions in the porous media [4]. If the pore space is occupied by the brine with high CO₂ concentrations, the dissolution rates will be reduced, increasing the time spans of the CO₂ precipitation from hundreds to thousands of years. Depending on

the stage of CO₂ sequestration and the physical properties of the saline aquifers, diffusion, advection, and convection can occur during the mass transport [5]. Through these mechanisms, the CO₂ near the two-phase interface is dissolved and transported away. Then, further fresh brine imbibes into the in situ pores and sequentially makes contact with free-phase CO₂, accelerating the dissolution process.

To determine the dissolution rate of the injected CO₂, scaling analysis based on simulation and experiments of the convective mixing and non-equilibrium imbibition have been applied to characterize the effect of convection and diffusion [6–8]. In previous studies, the dissolution process was widely investigated between the non-wetting phase (air/non-aqueous phase liquid) and the nearby wetting phase (water/brine) in porous media. For the observation focused on a single pore or a cluster and connected pore throats, the dissolution is dominated by molecular diffusion and mass transfer at the CO₂–water interfacial area [9]. Besides, in a 2-D model, the observed convection and dissolution rates are mainly an effect of dispersion due to the transport velocity of the solvent phase.

Dynamic measurement of the dissolution process is necessary to determine the potential impacts of the above mechanisms on the dissolution rate. During the CO₂ dissolution, brine saturated with CO₂ will be removed more effectively from the CO₂-brine interface and more unsaturated brine comes into contact with the CO₂. This process will be affected by the actual formation environment, including the reservoir temperature and pressure, flow development, heterogeneity, pore structure, and gas distribution [10]. In addition, the flow rate of the brine in the aquifer could be regarded as constant, while in the background, the flow CO₂ plume pushes the in situ brine to move forward at different flow rates. Thus, different CO₂ injection rates will result in the various dissolution rates of CO₂ at the field scale. Despite its recognized importance, measurement of the accurate dissolution rate of CO₂ into brine in realistic subsurface conditions is challenging due to the difficulty of conducting large-scale numerical simulations and experiments with reservoir complexity [11–13].

As the depth of target reservoir increases, CO₂ turns into the supercritical state because temperature and pressure surpass the critical point of the gas. In this state, compared to gaseous CO₂, supercritical CO₂ exhibits unique characteristics such as a high density, low viscosity, and high diffusivity and solubility. However, the studies of the effect of CO₂ phase state on dissolution rate are insufficient. For a given CO₂ droplet, the dissolution rate depends on the gas pressure and the fluid pair composition in the aquifer [14], while the dissolution rate of the CO₂ plume is sensitive to the density distribution inside the underground layer [15]. In the deep saline aquifer, the migration of denser fluid enhances CO₂ dissolution and brings in the trapping mechanism of density-driven convection between the gas plume and the CO₂-saturated brine. Meanwhile, higher diffusivity generally supports solubility trapping [16]. When the CO₂-brine system is strongly dispersive, more CO₂ will dissolve into the brine, and the dissolution process will be accelerated [17]. As the CO₂ solubility is enhanced under a supercritical state, it is expected that increasing pressure in deeper aquifers can greatly promote the solubility of CO₂ in aqueous solution [18]. Therefore, an adequate reservoir condition is important to reduce the time span of solubility trapping and will increase storage security [19].

In this study, we performed comparison experiments to measure the dissolution rate of gaseous and supercritical CO₂ in brine in brine-saturated porous media. The sand-filling core was pre-saturated with supercritical CO₂, followed by the brine injection, to dynamically characterize the two-phase dissolution. The process was reproduced with gaseous CO₂ to quantify the impact of the phase state on the dissolution rate. The micro-computed tomography (micro-CT) was applied to observe and measure the dynamic CO₂-brine dissolution, and visualized the flow development and distribution at different periods of CO₂ dissolution under supercritical and gaseous states. The CO₂ dissolution rates were analyzed with the porosity, CO₂ saturation, and the Reynolds number of the injected brine since the factors mainly contribute to the two-phase dissolution during the flow development in heterogeneous porous media.

2. Materials and Methods

2.1. Experimental Material and Performance

The porous media was un-consolidated glass beads (average particle diameter of 0.35–0.45 mm, As-one, Inc., Osaka-shi, Japan) packed in the vertical sand-pack holder. To simulate the reservoir condition, the temperature and pressure were maintained at 40 °C and 8 MPa, and CO₂ was under a supercritical state. The condition corresponds to the depth of 800 m for a typical geological reservoir. Also at room T&P conditions (25 °C and 0.1 MPa), CO₂ under a gaseous state was injected into the holder as the non-wetting phase for comparisons. The brine we employed in the experiments contained 3 mass % of NaCl (Analytical reagent AR, Tianjin Kemiou Chemical Reagent Co., Ltd., Tianjin, China) to simulate the subsurface salinity. Additionally, potassium iodide (KI, Analytical reagent AR, Tianjin Kemiou Chemical Reagent Co., Ltd., Tianjin, China) was dissolved in the brine as a contrast agent to enhance the contrast between brine and gas in the CT images, and the KI concentration was 6 mass %.

The experimental setup is shown in Figure 1. It consisted of a micro-X-ray CT scanner (InspeXio SMX-225CT, Shimadzu, Kyoto, Japan), syringe pumps, core holder, and temperature system. Three syringe pumps (260D, Teledyne ISCO Inc., Lincoln, NE, USA) were used in this system. Two syringe pumps injected brine and gas into the porous media and another syringe pump controlled the back pressure to keep the pressure stabilized throughout the experiments. The packed bed was 32 mm in length and 6 mm in diameter. A simple holder was fabricated from PEEK and stainless steel. The thickness of its wall was 3 mm. By using water-warmed temperature jackets, the temperature of the three syringe pumps was kept at the configured temperature, and an electric heating tape was used to control the temperature of core holder. The core holder, syringe pumps, and experimental pipelines were all wrapped in heat insulation cotton.

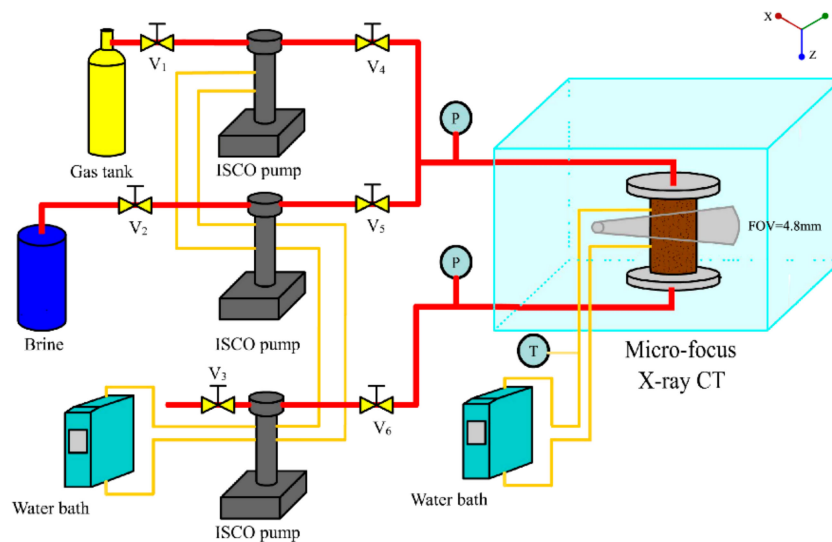


Figure 1. Experimental apparatus. The syringe pumps, ISCO pumps, were used as injection pumps and back pressure pump. The micro-computed tomography (Micro-focus X-ray CT) was configured under the same parameters between different sets of experiments. The length of the FOV (field of view) of the packed beads was 4.8 mm.

2.2. Experimental Procedure

Porous media was filled into the holder that was dried and vacuumed for a long time. CO₂ was injected into the system at a relatively low flow rate. When the temperature and pressure were kept stable for 2 h, the porosity and the original CO₂ distribution were acquired with the CO₂ saturated scan. Then, brine without saturated CO₂ was injected downward into the holder, and the flow rate remained

constant at 0.04 mL/min. Series of CT scans were conducted during these injections. Since the brine injection and the CT scan were performed simultaneously, the non-wetting phase could be changed dynamically, and CO₂ was constantly dissolved into the brine flow. Each experiment was run for several hours until the variation in the CO₂ saturation was less than 1%. We obtained 308 slice images with a cross-sectional area of 512 × 512 pixels for each slice, and the thickness of each slice was 16 μm. The length of the FOV (field of view) was 4.8 mm and located at the middle-upper part of the holder to prevent the end effect and allow the fluid flow to fully develop. In these experiments, scanning was performed at 90 kV and 50 μA. The spatial resolution was 16 μm/voxel.

3. Results and Discussion

In our experiments, the unsaturated brine was injected into the CO₂-saturated core at a Darcy velocity of 2.04 m/d. With similar core characteristics, the injection flow rate was much lower than the velocities in the dissolution experiment in the literature [9]. Therefore, the dissolution mechanism dominated during the brine imbibition and CO₂ gradually dissolved in the pore space as the brine injection continued.

3.1. Pore-Scale CO₂ Dissolution and Flow Development

The time-lapse images of CO₂-brine dissolution were rendered for selected slices, as shown in Figure 2. It is demonstrated that the overall dissolution rates are sensitive to the aqueous flow field, which was affected by the CO₂ distribution and the resulting reductions in relative permeability [20,21]. In the first few pore volumes (PV), the brine invaded along the side of the core and formed a continuous flow path. With the continuous injection of brine, the flow path expanded radially and stretched to the surrounding pores. The flow development in the downward imbibition was severely affected by the gravity effect, and flow bypassing occurred. A small amount of brine intruded into other areas of the core and formed film flow on the surface of the wetting porous media. The film water and corner flow in the former PV resulted in the swelling of thin film within pores and subsequent fragmentation of CO₂ droplets (shown in Figure 2 R1). The water flow between CO₂ bubbles and pore walls was found to affect the CO₂ dissolution rate [22]. In this period, the dissolution rate was controlled by the extension of the flow path. The fundamental reason for this is that further dissolution based on flow development was hindered by the pore structure under the gravity effect. The critical time of the dissolution rates was observed to be extremely sensitive to the position and size of the heterogeneous region, suggesting the disruption of the pore structure to the phase equilibrium [23].

The dissolution expansion was initiated at about 9.48 PV, and the duration was about 3 PVs. The brine began to invade the pores in the center of the core and formed multiple fingerings. With the branching and expansion of the fingerings, the large CO₂ cluster dissolved rapidly in the brine, significantly enhancing the CO₂ dissolution rate (shown in Figure 2 R2). Dissolution fingering may occur at CO₂-brine interfaces because of instabilities in CO₂ saturation and flow development during dissolution, as observed in a homogeneous pore network [24] and heterogeneous porous media [25]. High contact between the injected brine and the CO₂ surface (i.e., low bypassing) resulted in a greater CO₂ dissolution rate (shown in Figure 2 R3). Particularly for supercritical CO₂ under larger buoyancy forces, the faster growth of perturbations existed over time, which can provoke a more complicated structure of fingers and also more CO₂ dissolution into brine [17]. In contrast, the CO₂ bubbles located parallel to the flow direction led to more bypass trapping and lower average effluent concentrations [26]. The CO₂ bubbles, which were bound by the bypass flow, generally had low connectivity to the surrounding brine, or were isolated in the large pores through the connected pore throats (shown in Figure 2 R4). The flow bypassing was found to restrain the dissolution rate in experiments with CO₂ confined to the central region in the sand-filling core. Simultaneously, the brine that already occupied some corners of the pore gradually filled the pore space owing to the diffusion of the CO₂ in the brine (shown in Figure 2 R5). When the brine filled the upstream pores, some of the downstream bubbles happened to snap-off, and the detached part then rapidly dissolved (shown

in Figure 2 R6 and R7). The flow development and the diffusion and the coupled water flow and dissolution at the pore scale enhanced the dissolution rate at the pore-network scale, shortening the total depletion time of CO₂ [9,27].

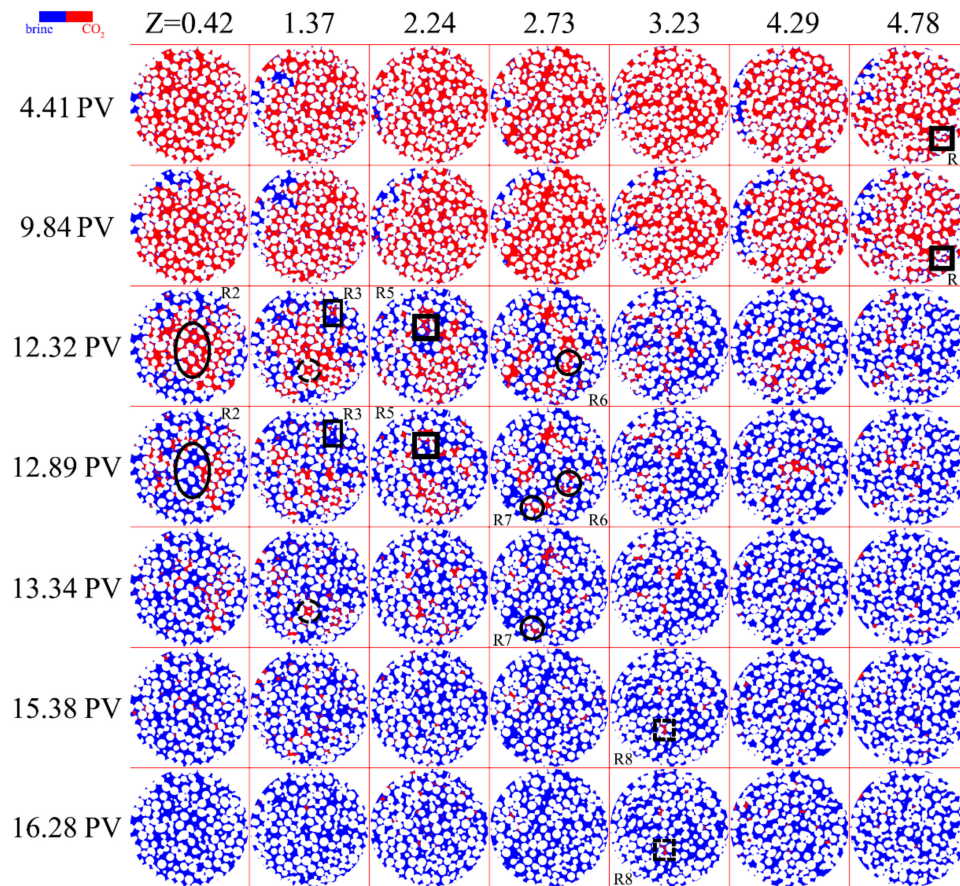


Figure 2. Time-lapse images of the supercritical CO₂ (red) at different positions for 0.04 mL/min. The position of the image along the vertical direction of the brine injection is short as Z, which is also the distance from the inlet.

After the major CO₂ bulk dissolved, the remaining CO₂ bubbles were trapped in the unconnected pores. The effect of the diffusion mechanism on the dissolution rate was enhanced during this period. CO₂ clusters trapped in the large pores were split by brine and changed in size and shape (shown in Figure 2 R8). The newly isolated CO₂ singlet existed for 1–3 PV, while the bubbles that inherited from the period of rapid dissolution expansion sometimes persisted for more than 4 PV. These isolated bubbles reduced the overall CO₂ dissolution rate and prolonged the duration of complete CO₂ dissolution.

For brine imbibition in porous media saturated with gaseous CO₂, the dissolution process was sustained for longer due to the residue of small bubbles. The flow development was limited, and a major priority path formed. The duration of gaseous CO₂ dissolution expansion was almost the same as supercritical CO₂. However, the density difference between gaseous CO₂ and the brine is over two orders of magnitude smaller than the case in supercritical CO₂. This leads to the brine imbibition being more concentrated in the porous media, directly restricting the number of the fingering. Figure 3 intuitively shows the consequence of this. Along part of the holder wall, the brine formed the priority path under the gravity effect, which occurred during the cross-sectional expansion. It is observed that the brine imbibition mainly occurred at the center of the core, and the time node when the CO₂ bulk began to dissolve occurred much earlier than for the supercritical CO₂.

The thin-film flow led to the snap-off of the bubble connected in large pore clusters (shown in Figure 3 R1). Within 2 PVs, the dissolution expanded along the flow paths with rapid CO₂ dissolution in the brine. However, characteristics of flow development indicated that brine tended to avoid the gaseous CO₂ clusters, implying lower dissolution rates and less probability of dissolution events. In the previous study, imbibition of unsaturated brine was more focused and had a lower sweep efficiency [9]. Taking the efficiency into account, the comparison of our results indicates that the supercritical CO₂ demonstrates its superiority to improve the trapping efficiency of CO₂ sequestration during the imbibition. The brine failed to invade into some pores at the corner of the core, and the isolated bubble sometimes existed for more than 16 PV (shown in Figure 3 R2). The gaseous CO₂ singlet significantly prolonged the duration of the dissolution, which is harmful to the trapping security of the CO₂ sequestration.

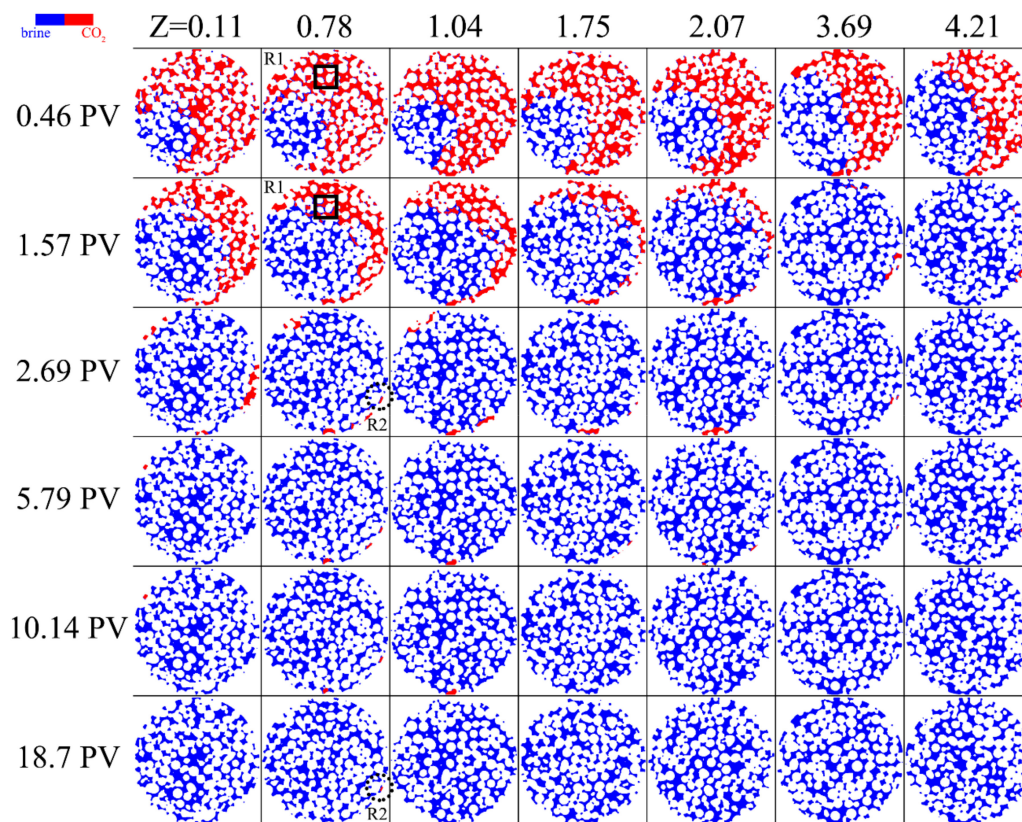


Figure 3. Time-lapse images of gaseous CO₂ (red) at different positions for 0.04 mL/min.

3.2. Porosity and Saturation Influence

The dissolution rate of CO₂ is defined as the CO₂ molar flux, which acts as an important indicator of the residual and solubility trapping mechanism [6]. The CO₂ dissolution is controlled by both diffusion and dispersion mechanisms, but the CO₂ dispersivity is commonly one to two orders of magnitude greater than the molecular diffusion coefficient. When brine imbibe to contact with CO₂, the dispersion between CO₂ and brine dominates and therefore the dissolution rate of this period is increased. As both dispersion and diffusion are active under a supercritical state, the dissolution rate follows the analogous definition of the pseudo-diffusion coefficient (Dps) which can be used for quantification of the dissolution rate of CO₂ in water [28]. In the case of the dissolution in porous media, it was calculated based on the rate of loss of CO₂ from the CO₂ phase,

$$Dps(x, t) = \frac{C(0, t)}{\Delta t} - \frac{\rho_g * \Delta\theta * \Delta x}{\Delta t^2 * U} \quad (1)$$

where $Dps(x, t)$ is the CO_2 dissolution rate, $C(0, t)$ is the concentration of CO_2 at the inlet of the core, Δt is the time interval of each CT scan, ρ_g is the CO_2 density, $\Delta\theta$ is the difference of CO_2 volume fraction, U is the Darcy flux, and Δx is the distance of brine imbibition below the inlet of the core.

The dissolution rate values at different PVs and their correlations with porosity are shown in Figure 4. The dissolution rate of supercritical CO_2 was about two or three orders of magnitude greater than that of gaseous CO_2 , indicating the prominent properties of the supercritical CO_2 during the dissolution process. In addition, the value distribution of the dissolution rate of CO_2 under the supercritical state was similar to that of gaseous CO_2 and spanned about four orders of magnitude. The dissolution rate of supercritical CO_2 increased as the flow path of the brine gradually expanded, and decreased as the isolated bubbles gradually dissolved due to the diffusion mechanism. By contrast, the dissolution rate of gaseous CO_2 dropped rapidly, and the value differences were approximately one order of magnitude at different PVs. This can be attributed to the difference in the critical time of dissolution expansion. In the cases of supercritical and gaseous CO_2 , the dissolution rate was maintained at a relatively large value during the domination of the dissolution expansion, and changed slightly with brine injection. Then, the dissolution rate of gaseous CO_2 decreased more dramatically because of the diverse number of residual CO_2 bubbles. The features correspond to the flow development which is shown in Figures 2 and 3.

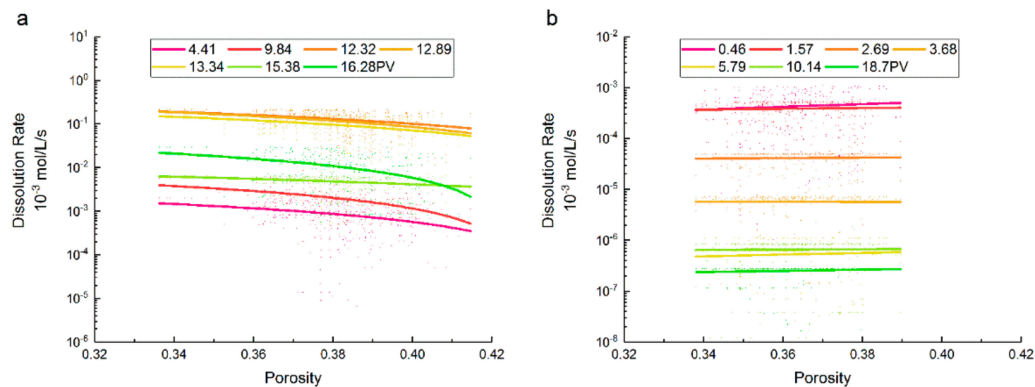


Figure 4. CO_2 dissolution rate vs. porosity at different injection PVs for (a) supercritical CO_2 and (b) gaseous CO_2 .

The porosity was defined by the following equation, as given in [29],

$$\varphi = \frac{V_c}{V} \tag{2}$$

where φ is the porosity, V_c is the void space in the pore structure, and V is the volume of the core sample. In our experiments, an adequate threshold was chosen to extract the pore space from the original CT images. The porosity profiles were generated from the CT scans of the dry core.

The dissolution rate of supercritical CO_2 decreased as porosity increased, and this trend increased with the increment of porosity. Simultaneously, the relatively small dissolution rate, which was located in the region of large porosity, decreased faster, and the descending trends between PVs had significant differences. In the previous study, a larger porosity heterogeneity may have led to more significant changes to the dissolution rate [30], while a simple relationship between the CO_2 -brine dissolution rate and cross-sectional area of adjoining pores would therefore not necessarily be expected [31]. This also proves the more active solubility of supercritical CO_2 .

The dissolution rate of gaseous CO_2 gradually increased with porosity, which showed no obvious effect on the variation of the dissolution rate. For both gaseous and supercritical CO_2 , no observable correlation existed between the ranges of the CO_2 dissolution rate and porosity at different PVs. However, when the porosity was between 0.36 and 0.38, the value ranges of dissolution rates under a

supercritical state were greater. It is suggested that pore-size distribution will affect the dissolution rate, which is another mechanism identified for trapping as varying solubility is applicable [32].

In previous studies, CO₂ saturation and the CO₂ reduction rate originating from the CO₂ dissolution are generally used to calculate the CO₂ capacity and trapping efficiency, respectively [1,10]. By using numerical analysis and resistivity monitoring, the computation of CO₂ saturation could be conducted. Also, the saturation could be indirectly obtained by isotope or acoustic data with accessible cost and convenient technicalities. The CO₂ saturation could be expressed as shown in Equation (3), based on the definition of porosity,

$$S_g = \frac{V_g}{\varphi} \tag{3}$$

where S_g is the CO₂ saturation, V_g is the volume of CO₂ phase, and φ is the porosity. As the CO₂ saturation increased, almost all CO₂ dissolution rates had slight variations. Consequently, after the saturation exceeded a certain threshold, the dissolution rate plummeted severely, which even varied from one to two orders of magnitude at the same PV. At high CO₂ saturations, concentration gradients were near zero because of the low velocities and prolonged contact with CO₂. This further reduced the active mass transfer from high saturation regions and illustrates the important role of low to medium saturations [20]. The plots of dissolution rate vs. saturation in Figure 5 were divided into two categories due to the significant differences of value ranges at different PVs, and the threshold of saturation was chosen as 0.1.

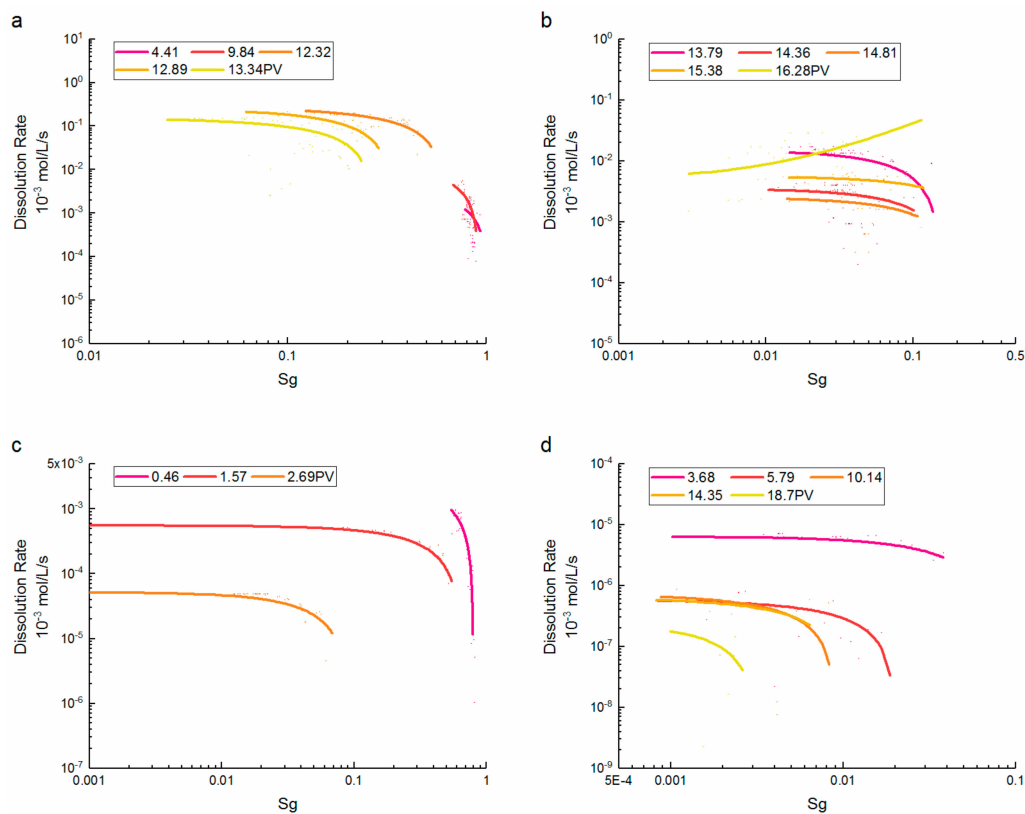


Figure 5. CO₂ dissolution rate vs. CO₂ saturation at different injection PVs for (a,b) supercritical CO₂ and (c,d) gaseous CO₂.

The dissolution rate of supercritical CO₂ increased with the saturation decreased, which was obviously reversed with the brine injection. The dissolution rate remained less than 6×10^{-6} mol/L/s before the brine formed multiple fingerings and increased rapidly with the saturation reduction. The observed growth in the CO₂ dissolution rate as the CO₂ saturation declined has been attributed to the creation of new water-flow paths as CO₂ was dissolved [33,34]. When CO₂ saturation was less than

0.5, the dissolution rate increased by two order of magnitude. At higher saturations, the dissolution rate may reduce by an order of magnitude, and the inverse correlation of the dissolution rate with the saturation remained invariant at a certain PV. This is because the smaller bubbles have higher dissolution rates than larger clusters [35]. In the saturations between 0.1 and 0.01, the correlations between the dissolution rate and saturation were inverted at later PVs. Subsequently, the dissolution rate was maintained at a relatively large level without monotonic decreasing with brine injection at the end of the dissolution process. Only a few bubble clusters remained in porous media, as shown in Figure 2. This suggests that the CO₂ dissolution rate is more vulnerable to being controlled by the location and quantity of the dissolution events. The distribution of the CO₂ phase and its contact area with the brine do influence the concentration gradient (driving force) at the CO₂-brine interface which, in turn, influences the dissolution rate [36,37]. The pore-scale variations of the flow field were found to significantly affect the dissolution rate of individual CO₂ bubbles, especially at low CO₂ saturations [38].

For gaseous CO₂, the dissolution rate was inversely proportional to CO₂ saturation. At higher saturations, the dissolution rate was relatively large. A smaller size of an initial CO₂ cluster will lead to more rapid dissolution [39]. The dissolution rate increased rapidly with the saturation reduction due to the rapid extension of the flow path with the brine injection. This indicates that entrapped CO₂ can result in preferential flow, flow paths can change with time as CO₂ dissolved, and the size and distribution of CO₂ bubbles at early PVs of imbibition affected the degree to which flow bypassing occurs. The relationships between the dissolution rate and saturation were close to supercritical CO₂ after saturations were less than 0.5. Meanwhile, when the saturations were between 0.001 and 0.1, the dissolution rates of CO₂ were dispersed between different saturations with differences of one to two orders of magnitude. It is reported that CO₂ dissolution rates are sensitive to pore scale variations in the size, shape, and spatial distribution of CO₂ bubbles [34]. In the period of residual bubble dissolution (especially at saturations less than 0.01), the dissolution rates were greater at the same PV if the bubbles in the porous media were smaller.

3.3. Reynolds Number-Dissolution Rate Relationships

The flow regime is characterized through the dimensionless number, the Reynolds number, which represents the ratio of the inertial force to the viscous force [40]. The equation of Re is written in the formula of,

$$\text{Re} = \frac{\rho_w * U * L}{\mu_w} \quad (4)$$

where ρ_w is the density of the brine, U is the Darcy velocity, L is the characteristic length, and μ_w is the viscosity of the brine. The Darcy velocity is proportional to the Reynolds number because the brine properties and the characteristic length are constant in the experiments. It is expected that the Darcy velocity will be affected by the saturation and the porosity at the pore scale. The Re was calculated for each position along the core since the geometry of the porous media is varied along the injection direction. In our experiments, the Re ranges from 0.001 to 1, which corresponds to laminar flows, so that the flow process was dominated by the viscous force [39].

In Figure 6, the order of the dissolution rate and the relevant range of Re varied widely at different PVs. Therefore, we adopt similar methods as the diagrams of the saturation–dissolution rate to distinguish the character of the dissolution rate when the Re distributions were concentrated in the later period of CO₂ dissolution. The corresponding linear relationships are presented visually in the insets.

In the early period of the supercritical CO₂ dissolution, the dissolution rate decreased with the increase of Re, and the relationship was reversed as most bubbles were dissolved. When the Re was greater than 0.1, the dissolution rate of supercritical CO₂ was relatively very small. This indicated that compared with the injection flow rate, the flow development critically determines the CO₂ dissolution in porous media. During the dissolution expansion, the dissolution rate increased rapidly

as the Re decreased, and the differences at different Re values were about one order of magnitude. The dissolution rates between solute and brine are highly variable in aquifers and depend on the flow rate of brine in the aquifer [41]. When buoyancy forces are preponderant (low injection flow rate), the dissolution rate increases with the distance of the brine imbibition, whereas a uniform dissolution could be observed at a high injection flow rate [42]. In the later period of dissolution, the Re was not greater than 0.01 at the same PV, but remained the order of magnitude similar to those in the early period of dissolution. In former studies, the highest dissolution rates were achieved during the injection and shortly after the injection periods, when CO_2 was still mobile and distributed over many pores before it settled underneath the caprock. The dissolution rate gradually increased with the Re , and the trend was not significantly correlated with the injected PV. This is similar to the process of phase equilibrium of CO_2 -brine in laminar flow. It is concluded that there is hardly any difference in dissolution rates between injection into a hydrostatic and a hydrodynamic aquifer, but with larger background flux, the dissolution rate may be higher [43]. Meanwhile, for CO_2 droplets, the dissolution rate increases with the flow velocity of brine, which is proportional to the Re [39].

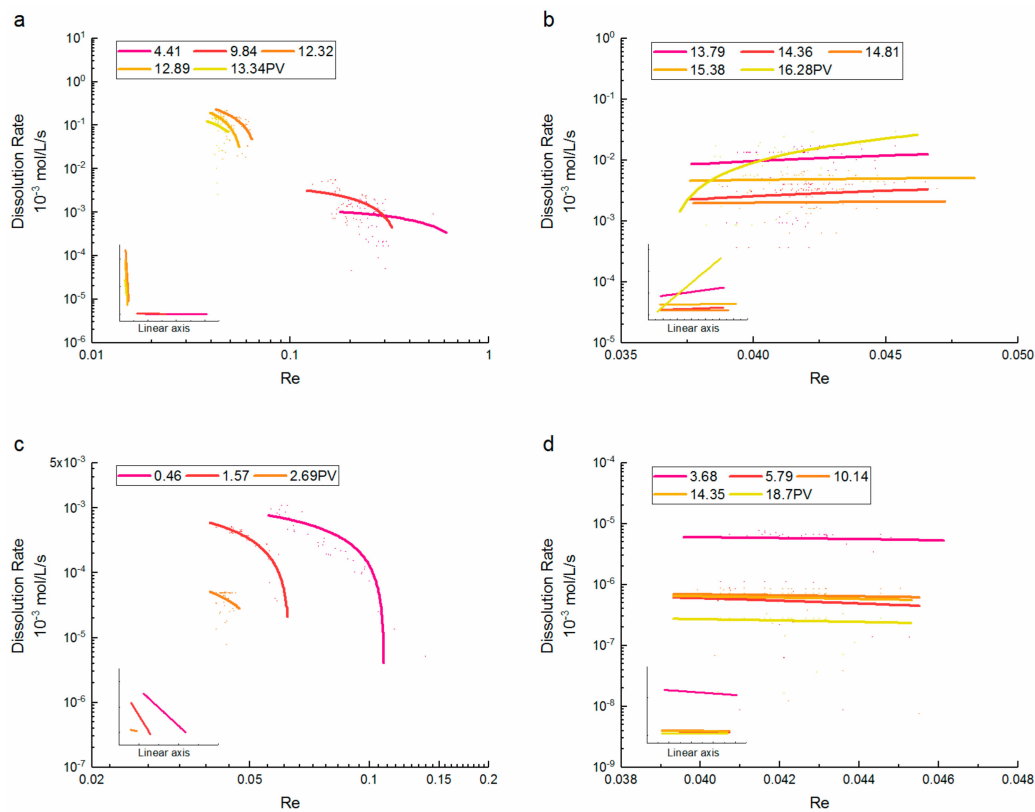


Figure 6. CO_2 dissolution rate at different Reynolds numbers for (a,b) supercritical CO_2 and (c,d) gaseous CO_2 .

When the Re was between 0.05 and 0.2, the dissolution rate of gaseous CO_2 significantly decreased with the increase of Re , and the dissolution rates were different by about two orders of magnitude at the same PV. Many bubbles resisted the accelerated dissolution; however, the overall dissolution rate for the CO_2 plume decreased with time because less CO_2 mass was associated with the dissolution [9]. The former studies showed that the initial dissolution rate constant depends on Re , the molecular diffusivity of CO_2 in water, and the mean pore size [44]. Thus, in certain cases with the combination of the influence factors, an increase in the flow rate resulted in no increase or a decrease in the dissolution rate [45]. The distribution of Re shrunk with the brine injection, and such a tendency was suspended with the decline of Re . In contrast with the case of supercritical CO_2 , the dissolution rate decreased

slightly at larger Re values in the later period of dissolution, whereas the differences in the dissolution rate between Re were inconspicuous.

4. Conclusions

The dissolution of the supercritical CO_2 in groundwater, which is referred to as CO_2 solubility trapping, is an important trapping mechanism of CO_2 geological storage in the deep aquifer. Considering the diffusion and dispersion of the CO_2 migration, an accurate measurement of the dissolution rate of CO_2 -brine at the pore scale is necessary to evaluate the dissolution process in the reservoir. In this study, the pore-scale dissolution rate during brine imbibition was calculated for both supercritical and gaseous CO_2 using X-ray computed microtomography. Also, we verified the different impacts of the porosity and saturation and the Reynolds number on both supercritical and gaseous CO_2 . The key novelties of the presented results in this study are summarized as:

- For flow development under a supercritical CO_2 state, high contact between the brine and CO_2 resulted in a greater CO_2 dissolution rate, while the flow bypassing restrained the dissolution rate with CO_2 confined to the central region. The detached part of the bubbles which happened to snap-off rapidly dissolved. The isolated bubbles reduced the overall CO_2 dissolution rate and prolonged the depletion time due to the slow diffusion. For gaseous CO_2 , the flow development was limited due to the greater density difference, implying lower dissolution rates and a lower probability of dissolution events. The isolated gaseous CO_2 existed for much longer and significantly prolonged the duration of the dissolution.
- The dissolution rate of supercritical CO_2 was about two or three orders of magnitude greater than that of gaseous CO_2 , while the value distributions both spanned about four orders of magnitude. The dissolution rate of gaseous CO_2 decreased more dramatically because of the diverse number of residual CO_2 bubbles.
- The dissolution rate of supercritical CO_2 decreased as the porosity increased, and this trend increased with the increment of porosity. The dissolution rate of gaseous CO_2 gradually increased with porosity, which showed no obvious effect on the variation of the dissolution rate. When the porosity is between 0.36 and 0.38, the value ranges of dissolution rates under a supercritical state were greater.
- At high CO_2 saturation, the dissolution rate of supercritical CO_2 increased rapidly with the saturation reduction. At low CO_2 saturation, the correlation between the dissolution rate and saturation was inverted at later PVs, and was controlled by the location and quantity of the dissolution events. By contrast, the dissolution rate of gaseous CO_2 remained inversely proportional to the saturation. However, the relationships were close to supercritical CO_2 after saturations were less than 0.5.
- During the dissolution expansion, the dissolution rate of supercritical CO_2 increased rapidly as the Re decreased, and the differences between Re were about one order of magnitude. At later PVs, the dissolution rate gradually increased with the Re , and the trend was not correlated with the injected PV. By contrast, the dissolution rate of gaseous CO_2 significantly decreased with the increase of Re . As most CO_2 was dissolved, the dissolution rate decreased slightly at larger Re values, whereas the differences between Re were inconspicuous.

Measurements from this study provided the relationship between parameters in the pore-scale flow regime. It is not evident that an upscaling simulation may readily import the dissolution rate results of this study to reservoirs. Also note that the effects of salinity and wettability on the CO_2 -brine dissolution process remain pertinent in porous media, which deserves further investigations.

Acknowledgments: This study has been supported by the National Natural Science Foundation of China (Grant No. 51506024), and the National Key Research and Development Program of China (Grant No. 2016YFB0600804). It has been also supported by the Fundamental Research Funds for the Central Universities (DUT16QY12).

Author Contributions: Bohao Wu conducted the experiments, analyzed the results, and drafted the manuscript. Xingbo Li, Yu Liu, and Lanlan Jiang conceived the experiments and reviewed the manuscript. Ying Teng, Pengfei Lv, and Tingting Luo designed and assisted the experiments. Jianan Zheng and Dayong Wang contributed materials.

Conflicts of Interest: We declare that we have no financial and personal relationships with other people or organizations that can inappropriately influence our work, there is no professional or other personal interest of any nature or kind in any product, service and/or company that could be construed as influencing the position presented in, or the review of, the manuscript entitled, "Characterizing dissolution rate of CO₂-brine in porous media under gaseous and supercritical conditions".

References

1. Woods, A.W. *Flow in Porous Rocks: Energy and Environment Applications*; Cambridge University Press: Cambridge, UK, 2015; pp. 1–289.
2. Zhang, S.; Xian, X.; Zhou, J.; Zhang, L. Mechanical behaviour of longmaxi black shale saturated with different fluids: An experimental study. *RSC Adv.* **2017**, *7*, 42946–42955. [[CrossRef](#)]
3. Wanniarachchi, W.; Gamage, R.; Perera, M.; Rathnaweera, T.; Gao, M.; Padmanabhan, E. Investigation of depth and injection pressure effects on breakdown pressure and fracture permeability of shale reservoirs: An experimental study. *Appl. Sci.* **2017**, *7*, 664. [[CrossRef](#)]
4. Mackay, D.; Matsugu, R.S. Evaporation rates of liquid hydrocarbon spills on land and water. *Can. J. Chem. Eng.* **1973**, *51*, 434–439. [[CrossRef](#)]
5. Guo, H.; Zhou, Q.; Wang, Z.; Huang, Y. Soret effect on the diffusion of CO₂ in aqueous solution under high-pressure. *Int. J. Heat Mass Transf.* **2018**, *117*, 966–971. [[CrossRef](#)]
6. Li, D.; Jiang, X.; Meng, Q.; Xie, Q. Numerical analyses of the effects of nitrogen on the dissolution trapping mechanism of carbon dioxide geological storage. *Comput. Fluids* **2015**, *114*, 1–11. [[CrossRef](#)]
7. Jiang, L.; Wu, B.; Song, Y.; Yang, M.; Wang, D.; Liu, Y.; Xue, Z. Mass transfer coefficient measurement during brine flush in a CO₂-filled packed bed by X-ray CT scanning. *Int. J. Heat Mass Transf.* **2017**, *115*, 615–624. [[CrossRef](#)]
8. Dou, B.; Zhang, H.; Cui, G.; Wang, Z.; Jiang, B.; Wang, K.; Chen, H.; Xu, Y. Hydrogen production and reduction of Ni-based oxygen carriers during chemical looping steam reforming of ethanol in a fixed-bed reactor. *Int. J. Hydrog. Energy* **2017**, *42*, 26217–26230. [[CrossRef](#)]
9. Chang, C.; Zhou, Q.; Kneafsey, T.J.; Oostrom, M.; Wietsma, T.W.; Yu, Q. Pore-scale supercritical CO₂ dissolution and mass transfer under imbibition conditions. *Adv. Water Resour.* **2016**, *92*, 142–158. [[CrossRef](#)]
10. Abidoye, L.K.; Khudaida, K.J.; Das, D.B. Geological carbon sequestration in the context of two-phase flow in porous media: A review. *Crit. Rev. Environ. Sci. Technol.* **2015**, *45*, 1105–1147. [[CrossRef](#)]
11. Zhao, J.; Wang, J.; Liu, W.; Song, Y. Analysis of heat transfer effects on gas production from methane hydrate by thermal stimulation. *Int. J. Heat Mass Transf.* **2015**, *87*, 145–150. [[CrossRef](#)]
12. Zhao, J.; Yu, T.; Song, Y.; Liu, D.; Liu, W.; Liu, Y.; Yang, M.; Ruan, X.; Li, Y. Numerical simulation of gas production from hydrate deposits using a single vertical well by depressurization in the Qilian Mountain permafrost, Qinghai-Tibet Plateau, China. *Energy* **2013**, *52*, 308–319. [[CrossRef](#)]
13. Zhao, J.; Zhu, Z.; Song, Y.; Liu, W.; Zhang, Y.; Wang, D. Analyzing the process of gas production for natural gas hydrate using depressurization. *Appl. Energy* **2015**, *142*, 125–134. [[CrossRef](#)]
14. Sun, R.; Cubaud, T. Dissolution of carbon dioxide bubbles and microfluidic multiphase flows. *Lab Chip* **2011**, *11*, 2924–2928. [[CrossRef](#)] [[PubMed](#)]
15. Song, Y.; Chen, B.; Nishio, M.; Akai, M. Experimental study of dissolution rate of a CO₂ droplet and CO₂ solubility in high pressure and low temperature seawater with hydrate free. In Proceedings of the ASME 2004 23rd International Conference on Offshore Mechanics and Arctic Engineering, Vancouver, BC, Canada, 20–25 June 2004; American Society of Mechanical Engineers: New York, NY, USA; pp. 301–307.
16. Ozgur, E.; Gümrah, F. Analytical and numerical modeling of CO₂ sequestration in deep saline aquifers. *Energy Sources Part A Recover. Util. Environ. Eff.* **2010**, *32*, 674–687. [[CrossRef](#)]
17. Ghesmat, K.; Hassanzadeh, H.; Abedi, J. The effect of anisotropic dispersion on the convective mixing in long-term CO₂ storage in saline aquifers. *AIChE J.* **2011**, *57*, 561–570. [[CrossRef](#)]
18. Pu, W.; Wei, P.; Sun, L.; Wang, S. Stability, CO₂ sensitivity, oil tolerance and displacement efficiency of polymer enhanced foam. *RSC Adv.* **2017**, *7*, 6251–6258. [[CrossRef](#)]

19. Ranganathan, P.; Farajzadeh, R.; Bruining, H.; Zitha, P.L.J. Numerical simulation of natural convection in heterogeneous porous media for CO₂ geological storage. *Transp. Porous Media* **2012**, *95*, 25–54. [[CrossRef](#)]
20. Kokkinaki, A.; O'Carroll, D.M.; Werth, C.J.; Sleep, B.E. Coupled simulation of dnapi infiltration and dissolution in three-dimensional heterogeneous domains: Process model validation. *Water Resour. Res.* **2013**, *49*, 7023–7036. [[CrossRef](#)]
21. Dou, B.; Zhang, H.; Cui, G.; Wang, Z.; Jiang, B.; Wang, K.; Chen, H.; Xu, Y. Hydrogen production by sorption-enhanced chemical looping steam reforming of ethanol in an alternating fixed-bed reactor: Sorbent to catalyst ratio dependencies. *Energy Convers. Manag.* **2018**, *155*, 243–252. [[CrossRef](#)]
22. Sahloul, N.A.; Ioannidis, M.A.; Chatzis, I. Dissolution of residual non-aqueous phase liquids in porous media: Pore-scale mechanisms and mass transfer rates. *Adv. Water Resour.* **2002**, *25*, 33–49. [[CrossRef](#)]
23. Green, C.P.; Ennis-King, J. Steady dissolution rate due to convective mixing in anisotropic porous media. *Adv. Water Resour.* **2014**, *73*, 65–73. [[CrossRef](#)]
24. Imhoff, P.T.; Miller, C.T. Dissolution fingering during the solubilization of nonaqueous phase liquids in saturated porous media: 1. Model predictions. *Water Resour. Res.* **1996**, *32*, 1919–1928. [[CrossRef](#)]
25. Farthing, M.W.; Seyedabbasi, M.A.; Imhoff, P.T.; Miller, C.T. Influence of porous media heterogeneity on nonaqueous phase liquid dissolution fingering and upscaled mass transfer. *Water Resour. Res.* **2012**, *48*. [[CrossRef](#)]
26. Agaoglu, B.; Scheytt, T.; Coptly, N.K. Impact of napi architecture on interphase mass transfer: A pore network study. *Adv. Water Res.* **2016**, *95*, 138–151. [[CrossRef](#)]
27. Sell, A.; Fadaei, H.; Kim, M.; Sinton, D. Measurement of CO₂ diffusivity for carbon sequestration: A microfluidic approach for reservoir-specific analysis. *Environ. Sci. Technol.* **2013**, *47*, 71–78. [[CrossRef](#)] [[PubMed](#)]
28. Nazari Moghaddam, R.; Rostami, B.; Pourafshary, P.; Fallahzadeh, Y. Quantification of density-driven natural convection for dissolution mechanism in CO₂ sequestration. *Transp. Porous Media* **2012**, *92*, 439–456. [[CrossRef](#)]
29. Wang, C.; Li, T.; Gao, H.; Zhao, J.; Li, H.A. Effect of asphaltene precipitation on CO₂-flooding performance in low-permeability sandstones: A nuclear magnetic resonance study. *RSC Adv.* **2017**, *7*, 38367–38376. [[CrossRef](#)]
30. Aggelopoulos, C.A.; Tsakiroglou, C.D. Effects of micro-heterogeneity and hydrodynamic dispersion on the dissolution rate of carbon dioxide in water-saturated porous media. *Int. J. Greenh. Gas Control* **2012**, *10*, 341–350. [[CrossRef](#)]
31. Johns, M.L.; Gladden, L.F. Magnetic resonance imaging study of the dissolution kinetics of octanol in porous media. *J. Colloid Interface Sci.* **1999**, *210*, 261–270. [[CrossRef](#)] [[PubMed](#)]
32. Emmanuel, S.; Ague, J.J.; Walderhaug, O. Interfacial energy effects and the evolution of pore size distributions during quartz precipitation in sandstone. *Geochim. Cosmochim. Acta* **2010**, *74*, 3539–3552. [[CrossRef](#)]
33. Nambi, I.M.; Powers, S.E. Napi dissolution in heterogeneous systems: An experimental investigation in a simple heterogeneous system. *J. Contam. Hydrol.* **2000**, *44*, 161–184. [[CrossRef](#)]
34. Zhang, C.; Werth, C.J.; Webb, A.G. A magnetic resonance imaging study of dense nonaqueous phase liquid dissolution from angular porous media. *Environ. Sci. Technol.* **2002**, *36*, 3310–3317. [[CrossRef](#)] [[PubMed](#)]
35. Karpyn, Z.T.; Piri, M.; Singh, G. Experimental investigation of trapped oil clusters in a water-wet bead pack using X-ray microtomography. *Water Resour. Res.* **2010**, *46*. [[CrossRef](#)]
36. Sale, T.C.; McWhorter, D.B. Steady state mass transfer from single-component dense nonaqueous phase liquids in uniform flow fields. *Water Resour. Res.* **2001**, *37*, 393–404. [[CrossRef](#)]
37. Lemke, L.D.; Abriola, L.M. Modeling dense nonaqueous phase liquid mass removal in nonuniform formations: Linking source-zone architecture and system response. *Geosphere* **2006**, *2*, 74–82. [[CrossRef](#)]
38. Johns, M.L.; Gladden, L.F. Surface-to-volume ratio of ganglia trapped in small-pore systems determined by pulsed-field gradient nuclear magnetic resonance. *J. Colloid Interface Sci.* **2001**, *238*, 96–104. [[CrossRef](#)] [[PubMed](#)]
39. Zendehboudi, S.; Khan, A.; Carlisle, S.; Leonenko, Y. Ex situ dissolution of CO₂: A new engineering methodology based on mass-transfer perspective for enhancement of CO₂ sequestration. *Energy Fuels* **2011**, *25*, 3323–3333. [[CrossRef](#)]
40. Elhalwagy, M.M.; Straatman, A.G. Dynamic coupling of phase-heat and mass transfer in porous media and conjugate fluid/porous domains. *Int. J. Heat Mass Transf.* **2017**, *106*, 1270–1286. [[CrossRef](#)]

41. Powers, S.E.; Abriola, L.M.; Weber, W.J. An experimental investigation of nonaqueous phase liquid dissolution in saturated subsurface systems: Steady state mass transfer rates. *Water Resour. Res.* **1992**, *28*, 2691–2705. [[CrossRef](#)]
42. Oltéan, C.; Golfier, F.; Buès, M.A. Numerical and experimental investigation of buoyancy-driven dissolution in vertical fracture. *J. Geophys. Res. Solid Earth* **2013**, *118*, 2038–2048. [[CrossRef](#)]
43. Woods, A.W.; Espie, T. Controls on the dissolution of CO₂ plumes in structural traps in deep saline aquifers. *Geophys. Res. Lett.* **2012**, *39*. [[CrossRef](#)]
44. Kumar, G.S. Mathematical modelling on transport of petroleum hydrocarbons in saturated fractured rocks. *Sadhana* **2014**, *39*, 1119–1139. [[CrossRef](#)]
45. McDonnell, D.; D’Arcy, D.M.; Crane, L.J.; Redmond, B. A mathematical analysis of drug dissolution in the usp flow through apparatus. *Heat Mass Transf.* **2017**. [[CrossRef](#)]



© 2017 by the authors. Licensee MDPI, Basel, Switzerland. This article is an open access article distributed under the terms and conditions of the Creative Commons Attribution (CC BY) license (<http://creativecommons.org/licenses/by/4.0/>).